Two-Dimensional Electron Model for a Hybrid Code of a Two-Stage Hall Thruster

Diego Escobar and Eduardo Ahedo

***Abstract*—An axisymmetric model for magnetized electrons in a Hall thruster, to be used in combination with a particle-in-cell model for heavy species, is presented. The main innovation is the admission of exchanges of electric current at the chamber walls, thus making the model applicable to a larger variety of Hall thrusters. The model is fully 2-D for regular magnetic topologies. It combines an equilibrium law for collisionless dynamics along the direction parallel to the magnetic field with drift–fluid equations for perpendicular transport. These are coupled to sheath models for the interaction with different types of walls. The derivation of a parabolic differential equation for the temperature and the full computation of the electric field work improves clarity and accuracy over previous models. Simulations of a Hall thruster with an intermediate current-driving electrode, operating in emission, floating, and collection modes are presented. Enhancement of thrust efficiency is found for the electrode working in the high-emission mode if the magnetic field strength is adjusted appropriately. The two-stage floating mode presents lower wall losses, lower plume divergence, and higher efficiency than the equivalent one-stage configuration.**

***Index Terms*—Hybrid simulation methods, plasma–material interactions, plasma propulsion, two-fluid plasmas.**

I. Introduction

In RECENT years, plasma propulsion has become a true alternative in Europe and USA to chemical propulsion in medium-power (1–5-kW) space applications since important fuel savings are achieved and successful flight-demonstration missions (DeepSpace-1, Artemis, and SMART-1) have reduced the reluctance of operators to use this new technology. Hall thrusters are among the most developed concepts in plasma propulsion, thanks largely to the four-decade Russian research and flight experience on them. In addition, Hall thrusters can provide the optimal specific impulses needed for station keeping and other near-Earth missions. As flight opportunities and confidence increase, the span of Hall thruster applications and technical requirements increases too. Innovative research is focused now on Hall thruster designs for efficient dual-mode (high-thrust/high-specific-impulse) operation, long lifetime, and nominal discharge powers ranging from 100 W to 100 kW.

Multistage Hall thrusters are among the possible solutions proposed to meet some of these requirements [1], [2]. This type of thrusters uses additional electrodes on the chamber walls to control better the electric field. This would allow one to optimize the ionization and acceleration processes (thus increasing thrust efficiency), to extend the operational envelope of the thruster, or to reduce the plume divergence [3]–[7]. Further enhancement of thruster performances would be achieved using *active* electrodes, capable of injecting a secondary electron current into the chamber. Ahedo and Parra [1] have shown that an intermediate electrode located and biased conveniently can deliver part of the electron current required for ionization at a lower energy cost than the electron current from the external cathode, with the subsequent efficiency gain. However, recent experiments with active electrodes [4], [6], [8], [9] have been unable to increment noticeably the efficiency of one-stage (1S) thrusters. This lack of success is likely due to several facts, such as an improper design or operation parameters, technical complications canceling out any gain derived from two-stage (2S) operation, and an insufficient understanding of the physics of 2S discharges.

The diversity of new Hall thruster designs makes more imperative a deeper understanding of the complex interplay of physical phenomena taking place in them and the development of reliable models of the plasma flow. Hybrid (particle/fluid) models are nowadays the optimal simulation option in terms of implemented physics and geometry, computation time, and detailed results. The first 2-D hybrid model for Hall thrusters, called HPHall, was developed by Fife [10]. Heavy species (ions and neutrals) are treated with a specifically designed particle-in-cell (PIC) plus Monte Carlo collision (MCC) method, whereas a fluidlike model is used for magnetized electrons. HPHall needs less than 2 h of computation in a standard personal computer (PC) to simulate a 1-ms discharge, with 10^5 macroparticles, 10^3 cells, the real magnetic topology, and a geometrical domain that includes the thruster chamber and the exterior near plume. In contrast, the full-PIC code of Adam *et al.* [11] takes one month of computation time in a four-processor PC cluster to simulate a 0.1-ms discharge, with a 1-D magnetic topology and a simple annular domain.

The huge difference in computational resources between hybrid and full-PIC codes is mainly due to the fact that the former ones can apply the plasma quasi-neutrality condition, thus avoiding to work with cell sizes smaller than the Debye length and with time steps smaller than the inverse of the plasma frequency. Nonetheless, hybrid codes must solve the

Manuscript received November 18, 2007; revised February 19, 2008. Current version published November 14, 2008. This work was supported by the Ministerio de Educación y Ciencia, Spain, under Project ESP2007-62694.

D. Escobar is with the European Space Operations Center, European Space Agency, 64293 Darmstadt, Germany (e-mail: diego.escobar@esa.int).

E. Ahedo is with the Escuela Técnica Superior de Ingenieros Aeronáuticos, Universidad Politécnica de Madrid, 28040 Madrid, Spain (e-mail: eduardo.ahedo@upm.es).

Color versions of one or more of the figures in this paper are available online at http://ieeexplore.ieee.org.

Digital Object Identifier 10.1109/TPS.2008.2004227

Debye sheaths forming around the various chamber walls. These sheaths provide the *correct* physical connection between the walls and the quasi-neutral plasma, and sheath models determine the correspondence between the known boundary conditions at the wall and those to be applied at the edge of the quasi-neutral domain. Thus, sheaths are a central piece of the whole plasma model, which influence the structure of the plasma flow through controlling energy and momentum losses to the walls. Also, they influence the wall sputtering by affecting the energy and angle of ions impacting the wall.

The implementation of more consistent plasma–wall interaction models was the main goal of Parra *et al.* [12], when upgrading the code HPHall into HPHall-2, making use of the previous work by Ahedo *et al.* for fluid models [13]–[15]. The large sensitivity of the electron distribution function and the plasma response to the interaction with walls has been debated extensively [16]–[19], and plasma–wall modeling continues to be a central research line in Hall thrusters [20]–[22].

HPHall has been used to simulate several thruster prototypes [23]–[25], high-specific-impulse operation [26], and wall sputtering [27]–[30]. Also, HPHall has been the reference for other 2-D hybrid codes. Hagelaar *et al.* [31] use a very similar hybrid model except for, on the one hand, the implementation of a more efficient implicit algorithm for integration of the electron equations and, on the other hand, the use of simple "empirical" laws proposed by Boeuf and Garrigues [32] for wall interaction parameters, thus renouncing to model the sheath physics. The code of Scharfe *et al.* [33] is also very similar to HPHall except for a simplified quasi-1-D formulation for electrons. There, the sheath model of Barral *et al.* [17] is implemented, which coincides essentially with that of Ahedo [13].

HPHall-2 presents two practical limitations. First, it is limited to simulate thrusters with a regular magnetic topology (i.e., $B \neq 0$), since electron equations are solved in a reference frame tied to the magnetic streamlines, and therefore, it cannot deal easily with regions where magnetic streamlines intersect (unless the integration domain is split into several subdomains). This "magnetic" frame is used since the numerical integration of electron fluxes in the cylindrical frame (used by the PIC subcode) is strongly hindered by the large anisotropy of the electron conductivity tensor. In order to deal with singular magnetic topologies, Hagelaar [34] proposes a numerical scheme that determines correctly the parallel and perpendicular electron fluxes directly in the cylindrical frame. Pérez-Luna *et al.* [2] have upgraded the hybrid code of Hagelaar *et al.* by implementing that scheme, but they keep Boeuf's expressions for plasma–wall interaction. The new code is successfully applied to a Hall thruster with a singular magnetic topology.

HPHall-2 is also limited to simulate Hall thrusters with lateral dielectric walls, that excludes multistage thrusters and thrusters with metallic walls, such as the thruster-with-anode-layer (TAL) family. The main goal of the model presented here is to remove this limitation from the code. This requires one, first, to modify the electron quasi-neutral equations in order that they admit net exchanges of electric current at lateral walls. Second, and complementary to it, it requires one to derive sheath models that are suitable for each type of nondielectric walls that are being simulated.

The upgrading of the electron model has given us the occasion of revising its mathematical formulation. As a result, a simpler and more accurate formulation than the original one, with a fully 2-D description of electron variables, is presented here. The clear advantage (in practical terms) of hybrid codes versus full-PIC codes must not hide the limitations of a fluid approach when dealing with weakly collisional magnetized electrons, as it is the case. Nonlocal transport along magnetic lines and microscopic turbulence are examples of phenomena that are difficult to include consistently in fluid equations [34]. Hence, a brief revision of the main assumptions supporting (or setting the limits of) the fluidlike model is presented.

Finally, the new capabilities of the model will be illustrated with simulations of a thruster with an active electrode, placed at one chamber wall, and operating at different modes for the electric current exchanged with the plasma. The results compare well with those of the 2S axial fluid model of Ahedo and Parra [1]. These showed that thruster efficiency can increase significantly in the electron-emitting mode if the magnetic field strength is adjusted appropriately, without modifying the usual one-peak magnetic topology. On the contrary, they found the efficiency to decrease always in the electron-collecting mode. Pérez-Luna *et al.* [2] have simulated a laboratory 2S prototype with a two-peak magnetic topology. No efficiency gain over one stage is obtained, but simulations are mainly within the electron-collecting mode.

Provisional versions of the present electron model and 2S simulations were presented in conference papers [26] and [35]. Here, the new electron model is run together with a version of the PIC code that is more advanced than the one HPHall-2 in [12]; these PIC improvements are reported elsewhere [26], [36], [37].

The rest of this paper is organized as follows. Section II presents the general aspects of the hybrid model and the magnetic reference frame. Section III introduces the 2-D electron quasi-neutral model. Section IV discusses the different sheath models. Section V presents boundary conditions, numerical integration, and comparisons with other existing codes. Section VI presents simulations of 1S and 2S discharges. Conclusions are drawn in Section VII.

II. General Features of the Hybrid Model

HPHall is a time-dependent axisymmetric model of the plasma discharge in a Hall thruster from the anode to an external location, near the cathode neutralization surface [Fig. 1(a)]. Cylindrical variables (z, r, and θ) describe the physical space.

The Debye length is assumed to be much smaller than any other geometrical or plasma length, so that the plasma is quasi-neutral except in thin Debye sheaths around the chamber walls. The computational domain simulates the quasi-neutral plasma and considers the Debye sheaths as surface discontinuities. A separate subcode solves these sheaths for each type of wall (metallic, ceramic, etc.) and provides the appropriate conditions at the boundary of the quasi-neutral domain.

There are two quasi-neutral subcodes: a PIC one for the heavy species and a fluid one for the electrons. The PIC subcode

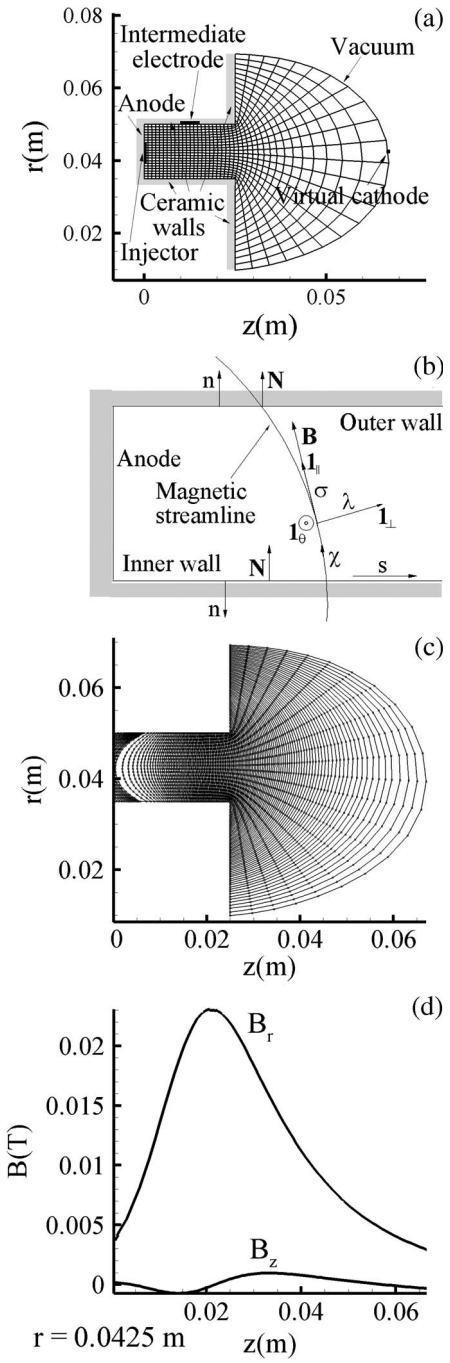

Fig. 1. (a) Elements of the simulated SPT-100-type thruster with an intermediate electrode, and the mesh used by the PIC subcode. (b) Elements of the magnetic-based reference frame. (c) Magnetic streamlines used as coordinate curves in the electron magnetic mesh, and nodes used in integrals along the streamlines. (d) Radial and axial components of the magnetic field at the chamber median.

deals with the following three different species: neutrals (n), singly charged ions (i_+), and doubly charged ions (i_{++}) [12], [36]. The PIC and electron subcodes are advanced sequentially in time with a time step Δt. In each temporal advancement, the electric potential and electron temperature fields ϕ and T_e are inputs of the PIC subcode and outputs of the electron subcode. Reciprocally, particle densities and fluxes of neutrals and ions are inputs of the electron subcode and outputs of the PIC subcode.

The magnetic field $\boldsymbol{B}$ is generated externally by the thruster magnetic circuit and is implemented into the simulation code in a preprocess. The small magnetic field induced by the discharge is negligible, so that $\boldsymbol{B}$ is irrotational and solenoidal. Magnetic potential and stream functions exist [$\sigma(r,z)$ and $\lambda(r,z)$, respectively], which satisfy

$$\begin{aligned} &\partial\sigma/\partial r = B_r, \quad \partial\sigma/\partial z = B_z \\ &\partial\lambda/\partial r = -rB_z, \quad \partial\lambda/\partial z = rB_r. \end{aligned} \tag{1}$$

The resulting orthogonal set of curvilinear coordinates is (λ,σ,θ), and the transformation between the Cartesian frame and the magnetic frame is

$$\begin{aligned} \boldsymbol{x}'_\lambda &= \frac{1}{rB^2}(-B_z\cos\theta, -B_z\sin\theta, B_r) \equiv \frac{\mathbf{1}_\perp}{rB} \\ \boldsymbol{x}'_\sigma &= \frac{1}{B^2}(B_r\cos\theta, B_r\sin\theta, B_z) \equiv \frac{\mathbf{1}_\parallel}{B} \\ \boldsymbol{x}'_\theta &= (-r\sin\theta, r\cos\theta, 0) \equiv r\mathbf{1}_\theta \end{aligned} \tag{2}$$

where $\{\mathbf{1}_\perp, \mathbf{1}_\parallel, \mathbf{1}_\theta\}$ is an orthonormal set [Fig. 1(b)]. The arc length along the streamlines, χ, is defined by

$$d\chi/d\sigma|_{\lambda=\text{const}} = B^{-1} \tag{3}$$

The set of curvilinear coordinates is considered to be regular out of the symmetry axis, which means that $B^2(z,r) > 0$ everywhere. For most Hall thruster geometries, it suffices to ask that $B_r(z,r) \neq 0$, such that $\partial\lambda/\partial z \neq 0$, and each streamline $\lambda(z,r)$ connects two different walls (or, more precisely, two different boundaries of the computational domain).

The particle and energy conservation equations for electrons have the functional form

$$\nabla\cdot\boldsymbol{p} = f \tag{4}$$

for certain functions $\boldsymbol{p}$ and f. The integral of this expression in a volume $\Delta\Omega$ bounded by two stream surfaces, λ and $\lambda+\Delta\lambda$, and *two lateral sheaths* of the thruster is

$$\begin{aligned} 0 &= \int_{\Delta\Omega} (\nabla\cdot\boldsymbol{p} - f)d\Omega \\ &= 2\pi \int_\lambda^{\lambda+\Delta\lambda} d\lambda' \left(\frac{\partial}{\partial\lambda'} \int_{\Gamma(\lambda')} d\chi r p_\perp + \sum_Q \frac{p_{nQ}}{\boldsymbol{B}_Q\cdot\boldsymbol{N}_Q} - \int_{\Gamma(\lambda')} d\chi \frac{f}{B} \right). \end{aligned} \tag{5}$$

Here, $p_\perp = \boldsymbol{p}\cdot\mathbf{1}_\perp$ and $p_n = \boldsymbol{p}\cdot\mathbf{1}_n$; $\mathbf{1}_n$ and $\boldsymbol{N}$ are unit vectors normal to a wall, pointing out of the volume and toward increasing radii, respectively. The volume differential element is $d\Omega = B^{-1}d\chi d\theta d\lambda$, and the surface differential element for a stream surface $S:\lambda(r,z) = \text{const}$ is $dS = |\boldsymbol{x}'_\sigma \times \boldsymbol{x}'_\theta| d\sigma d\theta = r d\chi d\theta$. If $\boldsymbol{r} = \boldsymbol{r}_w(s)$ represents the wall shape, with s being the arc length along the wall, one has $ds/d\lambda|_{\boldsymbol{r}=\boldsymbol{r}_w(z)} = (r\boldsymbol{B}\cdot\boldsymbol{N})^{-1}$. The subindex Q in the summation extends to the two sheath edges connected by one streamline, and $\Gamma(\lambda')$ means the streamline located at λ'.

The derivation of (5) with respect to $\Delta\lambda$ yields the λ-dependent 1-D integral transform of (4)

$$\frac{\partial}{\partial\lambda}\langle rBp_\perp\rangle = \langle f\rangle - \Sigma(p_n) \tag{6}$$

where the operators

$$\langle f\rangle = 2\pi \int\limits_{\Gamma(\lambda)} \frac{d\chi}{B} f \qquad \Sigma(p_n) = 2\pi \sum_Q \frac{p_{nQ}}{\boldsymbol{B}_Q \cdot \boldsymbol{N}_Q} \tag{7}$$

represent the integrals along the streamlines and the sum of fluxes *into the two lateral sheaths*, respectively. As a consequence of the curvature of the magnetic field, both operators include the magnetic field as a weighting function, and λ is the natural variable.

Finally, notice that for $B_z(z,r) = 0$ (radial streamlines) and $B_r(z,r) \propto r^{-1}$ (which satisfies $\nabla \cdot \boldsymbol{B} = 0$ but not $\nabla \wedge \boldsymbol{B} = 0$), (6) recovers the familiar cylindrical form

$$\frac{\partial}{\partial z} \int\limits_{\Gamma(z)} 2\pi r p_z = \int\limits_{\Gamma(z)} 2\pi r f dr - \sum_Q (2\pi r_Q p_{nQ}) \tag{8}$$

which is useful when comparing the present model with r-averaged radial ones.

III. 2-D Quasi-Neutral Model

A. Perpendicular and Parallel Dynamics

Electron dynamics are characterized by the following facts. First, electrons are highly magnetized, with a gyroradius ℓ_e being much smaller than the typical quasi-neutral plasma length (but still larger than the Debye length). Second, the thruster lateral walls effectively confine electrons except for a small collected fraction. Third, the electron collision time $\tau_{\rm col}$ (based on binary collisions mainly) is much shorter than the electron transit time in the channel τ_z (which is the confinement time too) but much larger than the bouncing time between lateral walls (τ_r) and the electron gyroperiod. These conditions justify, on the one hand, the adoption of a drift–fluid model for *perpendicular* electron transport, with a macroscopic velocity u_e being much smaller than the electron thermal velocity c_e. On the other hand, thermal equilibrium of confined electrons can be assumed for the near-collisionless parallel motion [38]. As a result, for large electron confinement, plasma density and potential satisfy the Maxwell–Boltzmann equilibrium law

$$n_e(\lambda,\sigma) = n_0(\lambda) \exp e\frac{\phi(\lambda,\sigma) - \phi_0(\lambda)}{T_e(\lambda)} \tag{9}$$

along the parallel direction. Here, $T_e(\lambda)$ is the electron temperature, and $\phi_0(\lambda)$ and $n_0(\lambda)$ are constants along each streamline, which will be chosen conveniently (in order to represent average values of density and potential in the streamline).

Perpendicular electron dynamics consist mainly of the azimuthal $\boldsymbol{E} \times \boldsymbol{B}$ drift plus the small axial drift. Condition $u_e \ll c_e$ is well satisfied except in very particular cases, like sharp localized peaks of $u_{\theta e}$ at the maximum of the electric field [39] or large u_e and $u_{\theta e}$ near positive anode sheaths [40] (not frequent in normal operation). In addition, azimuthal momentum convection must be taken into account for high secondary electron emission (SEE), when the exchange of magnetized primary electrons (p) by unmagnetized secondary electrons (s) at the walls causes a net loss of electron angular momentum $m_e n_e u_{\theta e}$.

Once the equilibrium law (9) has been established for parallel dynamics, and the PIC subcode provides the plasma density and other ion and neutral magnitudes, the electron perpendicular fluid model provides two equations for the conservation of particles and energy and four equations for the *perpendicular* transport of mass and heat. The set of seven equations determines totally the 2-D profiles of the electron temperature T_e, electric potential ϕ, thermalized potential ϕ_0, electron current density $\boldsymbol{j}_e$, and perpendicular heat conduction $q_{e\perp}\mathbf{1}_\perp + q_{e\theta}\mathbf{1}_\theta$. All these variables depend on λ and σ except for T_e and ϕ_0.

In Hall thrusters, there are two phenomena that can distort the simple equilibrium law (9). The first one is that the nonreplenishment of bulk electrons collected by the walls reduces the sheath potential fall formed around the wall. This produces a distribution function with a smaller "temperature" (i.e., velocity dispersion) in the parallel direction [22]. The second phenomenon is the presence, in the bulk of the plasma, of two near-free counterstreaming beams of SEE [18]. Nonetheless, (9) remains a reasonable approximation for parallel dynamics, since the temperature anisotropy is mild and the density of the SEE high-energy beams is small. There is not much difficulty in implementing a more elaborate equilibrium law for parallel dynamics, but this will be consistent only if the perpendicular fluid model takes into consideration that the distribution function is not close to a simple Maxwellian. Anisotropic magnetized fluid models are rather elaborate and include explicitly drift and mirror effects due to magnetic nonhomogeneities [41], [42].

It is worth pointing out that the Maxwell–Boltzmann equilibrium law (9) is satisfied also in the large-anisotropy limit of a *full* drift–fluid model for mass and heat transport, consisting of

$$\boldsymbol{j}_e = \bar{\bar{\sigma}} \cdot \left(-\nabla\phi + \frac{\nabla(n_e T_e)}{e n_e} \right) \tag{10}$$

$$\boldsymbol{q}_e = -\bar{\bar{\kappa}} \cdot \nabla T_e \tag{11}$$

with $\bar{\bar{\sigma}}$ and $\bar{\bar{\kappa}} = 5T_e\bar{\bar{\sigma}}/2e^2$ being the conductivity and thermal diffusivity tensors, respectively. For near-collisionless parallel dynamics, the parallel components of these two equations are acceptable only as numerical artifacts in order to fulfil the equilibrium law (9).

B. Current and Particle Conservation

The current density $\boldsymbol{j} = \boldsymbol{j}_i + \boldsymbol{j}_e$ satisfies

$$\nabla \cdot \boldsymbol{j} = 0 \tag{12}$$

which, in magnetic coordinates, becomes

$$\frac{\partial}{\partial\sigma}\left(\frac{j_\parallel}{B}\right) + \frac{\partial}{\partial\lambda}\left(\frac{r j_\perp}{B}\right) = 0. \tag{13}$$

Since the ion current density $\boldsymbol{j}_i$ is provided by the PIC subcode, this equation relates the parallel and perpendicular electron current densities $j_{e\parallel}$ and $j_{e\perp}$.

The integral transform of (12) yields the spatial evolution of the electron current $I_e(\lambda) = \langle rBj_{e\perp}\rangle$ across the streamlines

$$\frac{\partial I_e}{\partial \lambda} = -\frac{\partial I_i}{\partial \lambda} - \Sigma(j_n). \tag{14}$$

The electron continuity equation

$$\frac{\partial n_e}{\partial t} + \nabla \cdot (n_e \boldsymbol{u}_e) = \dot{n}_{\rm ion} \tag{15}$$

with $\dot{n}_{\rm ion}$ being the volumetric plasma source, will be used only as an auxiliary equation when computing the work of the electric field.

C. Perpendicular Transport of Mass and Heat

The perpendicular electron transport laws are coupled to the energy equation derived next. We summarize here the derivation made in [12].

The perpendicular fluxes of electrons satisfy the drift–diffusion equations

$$0 \simeq -rB\frac{\partial n_e T_e}{\partial \lambda} - en_e E_\perp - Bj_{e\theta} \tag{16}$$

$$0 \simeq Bj_{e\perp} - m_e \nu_{en} n_e u_{e\theta} + F_{\rm turb} - \left[\frac{D}{Dt}(m_e n_e \boldsymbol{u}_e)\right]_{\theta,p\to s} \tag{17}$$

where $\boldsymbol{E} = -\nabla\phi$ is the self-adjusted electric field, ν_{en} is the total electron–neutral collision frequency for momentum exchange, $F_{\rm turb}$ accounts for the turbulence effects from phase-correlated fluctuations of azimuthal forces [43], [44], and the last inertial term accounts for the azimuthal momentum losses caused by primary-to-secondary electron exchanges, also referred to as wall collisionality. References [12] and [14] discuss the transformation of these two effects in effective resistive terms, so that (17) is substituted by

$$j_{e\theta} = -\frac{\omega_e}{\nu_e} j_{e\perp}, \qquad \nu_e \approx \nu_{en} + \alpha_{\rm turb}\omega_e + \nu_{wm} \tag{18}$$

where ν_e is the effective collision frequency, with $\alpha_{\rm turb}$ measuring the relative turbulence level and ν_{wm} being the wall-collisionality frequency. The latter satisfies

$$\nu_{wm} \approx \frac{\Sigma\,(j^u_{sn})}{e\langle n_e\rangle} \tag{19}$$

with j^u_{sn} being the current density associated to *unmagnetized* secondary electrons from the wall (this includes diffusively backscattered primary electrons); notice that for zero secondary emission, one has $\nu_{wm} = 0$.

Parameter $\alpha_{\rm turb}$ is empirical in all Hall thruster models. At present, there is no theory that can establish and evaluate the (microscopic [11] or macroscopic [45]) mechanisms responsible for the turbulent-based perpendicular transport. Furthermore, there is even no consensus on an empirical expression for $\alpha_{\rm turb}(\lambda)$. It has been observed, quite obviously, that by tailoring appropriately that function, simulation profiles agree better with experimental ones, but different authors propose different expressions for $\alpha_{\rm turb}(\lambda)$ [33], [46]–[49]. Since this paper is not centered on the effects of turbulent diffusion, we assume simply that $\alpha_{\rm turb}$ is constant and the same for all simulations.

Equations (16) and (18) combine to yield Ohm's law for the perpendicular current density

$$j_{e\perp} = \sigma_\perp rB\left(-\frac{\partial\phi}{\partial\lambda} + \frac{1}{en_e}\frac{\partial n_e T_e}{\partial\lambda}\right) \tag{20}$$

with $\sigma_\perp = e^2 n_e \nu_e/(m_e\omega_e^2)$ being the perpendicular conductivity. Now, using the parallel equilibrium law (9) and choosing for n_0 the definition

$$n_0(\lambda) = \exp\frac{\langle\sigma_\perp r^2 B^2 \ln n_e\rangle}{\langle\sigma_\perp r^2 B^2\rangle} \tag{21}$$

the integral transform of (20) yields an equivalent Ohm's law

$$I_e = \langle\sigma_\perp r^2 B^2\rangle\left(-\frac{\partial\phi_0}{\partial\lambda} + \frac{1}{en_0}\frac{\partial n_0 T_e}{\partial\lambda}\right) \tag{22}$$

where the contributions of the "average" potential and pressure gradients are easily recognized. Using (9) and (22), (20) becomes

$$j_{e\perp} = \sigma_\perp rB\left(\frac{I_e}{\langle\sigma_\perp r^2 B^2\rangle} - \frac{1}{e}\frac{\partial T_e}{\partial\lambda}\ln\frac{n_e}{n_0}\right). \tag{23}$$

Using similar drift–fluid equations for the perpendicular heat transport, the heat-flux components satisfy

$$q_{e\theta} = -\frac{\omega_e}{\alpha_q\nu_e} q_{e\perp}, \qquad q_{e\perp} = -\kappa_\perp rB\frac{\partial T_e}{\partial\lambda} \tag{24}$$

where $\kappa_\perp = (\alpha_q 5/2)\sigma_\perp T_e/e^2$ is the perpendicular thermal diffusivity and the factor α_q accounts for differences in the effective collision rate for mass and heat transport (it is uncertain that turbulence and wall collisionality affect identically the two processes).

D. Work of the Electric Field

The energy equation includes the work of the electric field $\langle\boldsymbol{j}_e\cdot\boldsymbol{E}\rangle$. This can be decomposed in perpendicular and parallel contributions $\langle j_{e\perp}E_\perp\rangle$ and $\langle j_{e\parallel}E_\parallel\rangle$, respectively. Fife [10] disregards the parallel contribution, arguing that it is much smaller than other terms and requires one to compute the parallel current $j_{e\parallel}$, which otherwise is decoupled from the main set of equations. Both Hagelaar *et al.* [31] and Parra *et al.* [12] keep this simplification. Pérez-Luna *et al.* [2], who obtain $\boldsymbol{j}_e$ in the main integration scheme, seem to keep the parallel contribution.

Globally, the parallel work makes a small contribution to the energy balance, but the contribution can be comparable to other ones in certain cases. For instance, $E_\parallel$ tends to be larger than $E_\perp$ in the rear part of the Hall thruster chamber, and potential falls along the streamlines within the plasma bulk can be larger than in the adjacent sheaths if the tail of wall-collected

electrons is highly depleted [22] or for electron-collecting electrodes with magnetic streamlines parallel to the electrode (as found out by Ahedo and Escobar [40] around the anode or by Pérez-Luna *et al.* [2] around the intermediate electrode).

Furthermore, an exact derivation of $\langle \boldsymbol{j}_e \cdot \boldsymbol{E} \rangle$ in terms of suitable variables is rather straightforward. Using the identity

$$\langle \boldsymbol{j}_e \cdot \boldsymbol{E} \rangle = -\langle \nabla \cdot \phi \boldsymbol{j}_e \rangle + \langle \phi \nabla \cdot \boldsymbol{j}_e \rangle \tag{25}$$

and making an extensive use of (6) and previous equations for ϕ, I_e, and $j_{e\perp}$, one finds

$$\langle j_{e\perp} E_\perp \rangle = \frac{I_e^2}{\langle \sigma_\perp r^2 B^2 \rangle} - \frac{I_e}{e n_0} \frac{\partial n_0 T_e}{\partial \lambda} \tag{26}$$

$$\begin{aligned} \langle j_{e\parallel} E_\parallel \rangle = {} & \frac{\partial}{\partial \lambda} \left(\langle r^2 B^2 \kappa_E \rangle \frac{\partial T_e}{\partial \lambda} \right) \\ & + T_e \left\langle \left(\frac{\partial n_e}{\partial t} - \dot{n}_{\text{ion}} \right) \ln \frac{n_e}{n_0} \right\rangle \\ & - T_e \Sigma \left(\frac{j_{en}}{e} \ln \frac{n_e}{n_0} \right) \end{aligned} \tag{27}$$

with

$$\kappa_E = \sigma_\perp \frac{T_e}{e^2} \ln^2 \frac{n_e}{n_0} \tag{28}$$

being an associated thermal diffusivity. The assignment of terms of $\langle \boldsymbol{j}_e \cdot \boldsymbol{E} \rangle$ to the parallel and perpendicular contributions has been based on the fact that the variation of n_e along a streamline is due exclusively to $E_\parallel$ [(9)], so that $\langle j_{e\parallel} E_\parallel \rangle = 0$ if $\ln n_e$ were constant along a streamline.

The Joule heating and the work of the pressure perpendicular gradient are easily identifiable in the compact expression for the perpendicular electric work. The last contribution to the parallel electric work is the product of the electron current density to the lateral sheaths and an average potential fall along the streamline

$$- T_e \Sigma \left(\frac{j_{en}}{e} \ln \frac{n_e}{n_0} \right) = -2\pi \sum_Q \frac{j_{enQ}}{\boldsymbol{B}_Q \cdot \boldsymbol{N}_Q} (\phi_Q - \phi_0). \tag{29}$$

E. Energy Conservation

The total energy conservation equation in the drift-diffusive and isotropic-temperature limits is

$$\frac{\partial}{\partial t} \left(\frac{3}{2} n_e T_e \right) + \nabla \cdot \left(\frac{5}{2} T_e n_e \boldsymbol{u}_e + \boldsymbol{q}_e \right) = \boldsymbol{j}_e \cdot \boldsymbol{E} - \dot{Q}_{\text{inel}} \tag{30}$$

where $\dot{Q}_{\text{inel}}$ accounts for losses due to (single and double) ionization and radiation from electron de-excitation.

The integral transform of this equation yields the evolution equation for the internal energy density

$$\begin{aligned} \frac{\partial}{\partial t} \left(\langle n_e \rangle \frac{3}{2} T_e \right) - \frac{\partial}{\partial \lambda} \left(\frac{5 I_e}{2e} T_e - \langle r B q_{e\perp} \rangle \right) \\ = \langle \boldsymbol{j}_e \cdot \boldsymbol{E} \rangle - \langle \dot{Q}_{\text{inel}} \rangle - \Sigma(h_{en}) \end{aligned} \tag{31}$$

with h_{en} being the electron energy density flux into the two Debye sheaths (which differs generally from the flux into the walls).

Using (24), (26), and (27) for the heat flux and the electric field work, the integral transform of (31) yields a classical parabolic equation for the internal energy density

$$\begin{aligned} & \frac{\partial}{\partial t} \left(\langle n_e \rangle \frac{3}{2} T_e \right) - \frac{\partial}{\partial \lambda} \left(\frac{5 I_e}{2e} T_e \right) \\ & \quad - \frac{\partial}{\partial \lambda} \left(\langle (\kappa_\perp + \kappa_E) r^2 B^2 \rangle \frac{\partial T_e}{\partial \lambda} \right) \\ & \quad = -\langle \dot{Q}_{\text{inel}} \rangle + \frac{I_e^2}{\langle \sigma_\perp r^2 B^2 \rangle} - \frac{I_e}{e n_0} \frac{\partial n_0 T_e}{\partial \lambda} \\ & \qquad + T_e \left\langle \left(\frac{\partial n_e}{\partial t} - \dot{n}_{\text{ion}} \right) \ln \frac{n_e}{n_0} \right\rangle \\ & \qquad - T_e \Sigma \left(\frac{j_{en}}{e} \ln \frac{n_e}{n_0} \right) - \Sigma(h_{en}) \end{aligned} \tag{32}$$

with $\kappa_\perp + \kappa_E$ being the total thermal diffusivity (which is proportional to T_e).

Equation (32) completes the quasi-neutral formulation. Its standard expression, as a parabolic partial differential equation for T_e, improves the previous 2-D formulations in hybrid codes, which consisted in a temporal differential equation for T_e and $\partial T_e / \partial \lambda$ at discrete λ-nodes [10], [12], [31]. This discrete equation was derived working with the integral terms of (5) instead of using (6).

IV. Sheath Models

The quasi-neutral model includes the following three fluxes at the two sheath edges: j_{en}, j_{sn}, and h_{en}. These must be determined from appropriate sheath models for each type of wall or electrode in terms of variables of the quasi-neutral model. It turns out that these sheath models are *strongly coupled* to the quasi-neutral model and must be solved simultaneously; sometimes, this coupling leads to strong numerical instabilities.

Sheaths are also coupled with the PIC model for ions. In most cases, sheaths are *negative*, i.e., they are ion attracting and electron confining. Then, the sheath potential fall ϕ_{WQ} yields the gain of ion perpendicular energy within the sheath, which is necessary to compute the ion energy and angle at wall impact, wherefrom the wall sputtering is computed [28]. *Positive* sheaths present a stronger coupling with the PIC subcode, since they reflect back ions of low perpendicular energy. Positive sheaths also mean no electron confinement [40] and, therefore, more complex parallel dynamics for electrons. Positive sheaths are not common in Hall thrusters, but they are likely to form in front of an electrode with high electron collection.

Different models of negative sheaths are currently implemented in the hybrid code. First, there is the sheath model for a *metallic and current-driving electrode*, which is used for the thruster anode. The last version of this sheath model is reported in [50, Sec. II. A]. Second, there is a sheath model for a *dielectric wall and thermalized electrons*. This is basically the model of Ahedo [13], implemented in HPHall-2, with additional improvements on the electron distribution function, and the inclusion of double ions and supersonic ion velocities

at the sheath edge (these last ones arising from the time-oscillatory behavior of the quasi-neutral plasma [50]). There are two regimes in this model, depending on the sheath being or not *charge saturated*. Third, there is a sheath model for a *charge-saturated*, *current-driving electrode* (hereafter just called *active electrode*), which simulates a hot thermionic emitter or equivalent electrode. This will be used here for 2S discharges. Finally, there is a sheath model for a *dielectric wall and electron partial thermalization*, which considers that the distribution function of primary electrons at the wall is a partially depleted half-Maxwellian. First results with this last model confirm the large sensitivity of the plasma response to the depletion of the tail of collected electrons [49]. In particular, large reductions of the sheath potential fall and power losses to the lateral walls are found for 90% of tail depletion.

A. Models for Electron Total Thermalization

A comparison of the main features of the sheath models for different types of walls, and thermalized primary electrons is summarized here. For the sake of clarity, zero backscattering of electrons at the wall is assumed. A collisionless negative sheath between the wall W and the sheath edge Q is assumed. The sheath is monotonic with ϕ (except very near the wall in the charge-saturated regime), and the potential fall is ϕ_{WQ}. The following two populations of electrons are taken into account: the primary electrons (p) coming from the quasi neutral plasma and the secondary electrons (s) coming from the wall. Both populations are assumed to have a semi-Maxwellian distribution function at the wall with temperatures T_α's and densities $n_{\alpha W}$'s (where $\alpha = p, s$). The characteristics of the ion population at Q are known from the PIC subcode.

The current densities of the three species are constant within the sheath. The two electron currents are

$$j_{pnQ} = -en_{pW}\sqrt{\frac{2T_p}{\pi m_e}} \qquad j_{snQ} = en_{sW}\sqrt{\frac{2T_s}{\pi m_e}}. \tag{33}$$

The electron total energy fluxes at W and Q are

$$\begin{aligned} h_{enW} &= -\frac{2}{e}(T_p j_{pnQ} + T_s j_{snQ}) \\ h_{enQ} &= h_{enW} - \phi_{WQ} j_{enQ}. \end{aligned} \tag{34}$$

The electron density within the sheath is

$$\begin{aligned} n_e(\phi) = n_{pW} \exp\frac{e\phi - e\phi_W}{T_p}\left(2 - \operatorname{erfc}\sqrt{\frac{e\phi - e\phi_W}{T_p}}\right) \\ + n_{sW} \exp\frac{e\phi - e\phi_W}{T_s}\operatorname{erfc}\sqrt{\frac{e\phi - e\phi_W}{T_s}}. \end{aligned} \tag{35}$$

From a first integral of Poisson's equation, the electric field in the sheath, $E_n = -\partial\phi/\partial \mathbf{1}_n$, satisfies (in the length scale associated to the Debye length)

$$E_n^2 \simeq \frac{2}{\epsilon_0}\int_{\phi}^{\phi_Q} (\rho_i - en_p - en_s)\, d\phi \tag{36}$$

with $\rho_i(\phi)$ being the ion electric charge. Charge saturation (CS) conditions are obtained when the electric field at the wall becomes zero, which is for

$$e\int_{\phi_W}^{\phi_Q} (n_p + n_s) d\phi = \int_{\phi_W}^{\phi_Q} \rho_i\, d\phi. \tag{37}$$

At the CS limit, the total electric charge within the sheath is zero, and the sheath becomes a double layer [51]. Beyond the CS limit, a potential well (on the order of T_s/e) is formed in order to reflect back to the wall part of the electron wall emission. In this way, the potential well acts as an automatic control of the secondary emission that reaches the quasi-neutral plasma. In general, T_s is small compared to the sheath potential fall, and the *dimensionless* sheath solution within the CS regime is the one at the CS limit.

The temperature of secondary electrons (T_s) is considered known (∼1–3 eV). Then, four conditions are needed in order to determine ϕ_{WQ}, T_p, n_{pW}, and n_{sW}. Two of them are related to the fact that electrons are modeled with a single population (e) in the quasi-neutral plasma and with two populations inside the sheath. The continuity of n_{eQ} and $(\partial n_{eQ}/\partial\phi)_Q$ using (9) and (35) at each side of the sheath edge is needed to assure a good matching of electron flow properties [13].

The other two conditions depend on the type of wall. For a *dielectric material*, we have the following: 1) The electric current is zero $(j_{inQ} + j_{enQ} = 0)$, and 2) the SEE yield curve of the material $\delta_{sp}(T_p) \equiv -j_{snQ}/j_{pnQ}$ is known. For each material, the sheath reaches the CS limit at certain temperature (T_p^*). For a *CS dielectric wall*, which is for $T_p > T_p^*$, the last condition becomes $-j_{snQ}/j_{pnQ} = \delta_{sp}(T_p^*)$. For an *active electrode*, where electron emission is limited by CS conditions at the electrode surface, the following are noted: 1) The CS condition (37) is imposed, and 2) either j_{nQ} or ϕ_W is known. For a *metallic material*, we normally impose the following: 1) SEE is negligible, and 2) ϕ_W is known.

Electron fluxes and sheath potential falls for dielectric walls with different SEE yields (and electron total thermalization) are given in [13]. For a dielectric material with a crossover temperature T_1 for the SEE yield, the contributions to the term $\sum(h_{en})$ for energy losses at the sheath edges in (32) scale as

$$h_{enQ}(T_e, T_1) \propto n_{eQ} T_e^{3/2} \times \beta(T_e/T_1) \tag{38}$$

with β being about 15 times larger for CS conditions than for zero SEE [13], [17]. In the case of electron partial thermalization, the scaling law (38) continues to be valid, with β decreasing as the thermalization mean free path increases [22].

Fig. 2 shows electron fluxes and sheath potential falls for an active electrode and simple ion flow conditions. Although the electrode is always an emitter of secondary electrons $(j_{snQ} > 0)$, the sign of the net electric current distinguishes the floating $(j_{nQ} = 0)$, collection $(j_{nQ} < 0)$, and emission modes $(j_{nQ} > 0)$ of operation (notice that the usual convention in terms of the negative electric current is used). In all modes, the electron fluxes are much larger than the ion flux: $j_{pnQ} \simeq j_{snQ} \gg j_{inQ}$. In general, we expect the active electrode to operate with

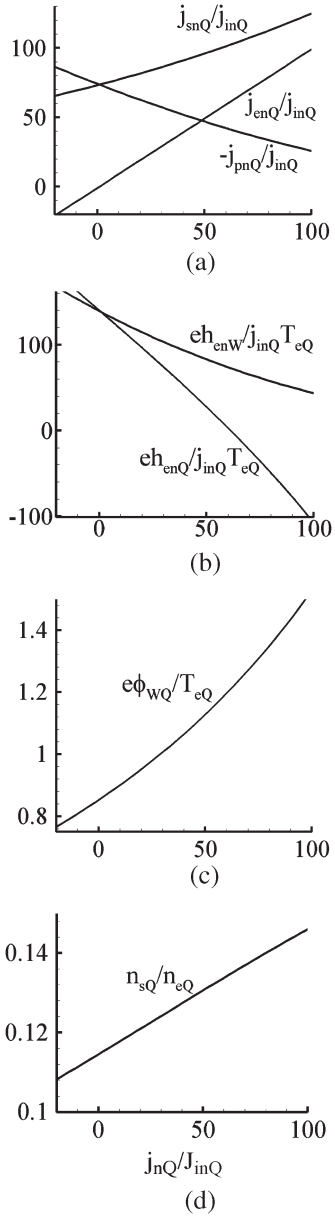

Fig. 2. Characteristics of an electron-emitting electrode in terms of the total-current-to-ion-current ratio. (a) Nondimensional primary, secondary, and net electron currents. (b) Nondimensional energy fluxes into the sheath and the wall. (c) Nondimensional sheath potential fall. (d) Nondimensional secondary electron density in the sheath edge. All results shown are computed assuming a sonic ion flux composed only by singly charged cold ions and zero secondary electron temperature.

$e\phi_{WQ}/T_e \sim 1$ and $T_s \ll T_p$. Then, secondary emission makes a small contribution to the plasma density in the quasi-neutral region, $n_{sQ} \ll n_{eQ}$, and to energy wall losses. On the contrary, it contributes strongly to decrease the energy flux at the sheath edge in the emission mode, which can be expressed as

$$h_{enQ}(T_e, j_{nQ}) \simeq \frac{T_e}{e}\left(2|j_{pnQ}| - \frac{e\phi_{WQ}}{T_e} j_{nQ}\right) \tag{39}$$

or, using a linear fitting from numerical results, as

$$\frac{eh_{enQ}}{T_e j_{inQ}} \approx 140 - 2.3\frac{j_{nQ}}{j_{inQ}}. \tag{40}$$

The energy flux into the sheath changes from positive to negative for $j_{snQ}/|j_{pnQ}| \sim 2.44$, which corresponds to $j_{nQ}/j_{inQ} \sim 61.2$. Therefore, an active electrode in the high-emission mode (which can be defined vaguely by $j_{nQ}/j_{inQ} > 100$) *heats* the quasi-neutral plasma at a rate of $h_{enQ}(T_e, j_{nQ}) \sim -\phi_{WQ} j_{nQ}$.

V. Closure of the Electron Model

Once the sheath models are matched, (9), (14), (22), and (32) constitute a closed set of coupled equations for $T_e(\lambda)$, $I_e(\lambda)$, $\phi_0(\lambda)$, and $\phi(\lambda, \sigma)$ in terms of magnitudes known from the PIC subcode. Once these magnitudes are known, the three components of $\boldsymbol{j}_e(\lambda, \sigma)$ come out from (18), (23), and the integration of (13) along each streamline.

A. Boundary Conditions

The electron model equations require four conditions at the boundary streamlines: λ_A in the anode side and λ_P in the near plume. Normally, these conditions are I_{eP}, T_{eP}, $(\partial T_e/\partial\lambda)|_A$, and the point of zero potential. The virtual cathode is chosen as the zero potential point, and then, the potential at the metallic anode coincides with the discharge potential, V_d. Additionally, (13) requires the boundary condition

$$j_{e\|Q} = \left.\frac{j_{en} - j_{e\perp}\mathbf{1}_\perp \cdot \mathbf{1}_n}{\mathbf{1}_\| \cdot \mathbf{1}_n}\right|_Q \tag{41}$$

at the sheath edge where the integration starts; the fulfillment of (14) assures that the same condition is satisfied automatically at the other sheath edge.

There are several issues related to the anode and cathode boundaries that are discussed hereafter. The closure of (14), (22), and (32) at the anode is delicate since, first, the anode surface does not coincide with a streamline generally, and second, the sheath is nonuniform, with its parameters (potential fall, current density, etc.) varying along the anode surface. The treatment of the region lying between the anode and the streamline tangent to it (the "separatrix") is discussed in [37, Sec. II]. Basically, the procedure consists of the following: 1) A streamline intersecting the anode is used in order to define an effective value of λ_A and integrate the aforementioned equations on λ; 2) plasma variable values at the sheath edge are obtained by usual bilinear interpolation; and 3) at each anode point, the anode sheath model is used to relate edge and wall magnitudes. In certain magnetic topologies [25], the region between the anode and the separatrix is quite large, and the accuracy of the solution is reduced there.

The difficulties at the anode suggest that, whenever possible, the plume boundary λ_P should coincide with a magnetic streamline. Then, a "cathode model" for the neutralization of the ejected ion beam must be formulated. The simplest model consists of taking the streamline λ_P as the one intersecting the cathode. Then, T_{eP} is the emission temperature, and

$$I_{eP} = I_P - I_{iP} \tag{42}$$

with I_P being the discharge current delivered by the external circuit through the cathode. In a thruster without internal electrodes, I_P is the discharge current at the anode (I_d). If the external electric circuit fixes the discharge current I_d, two iterations are needed to adjust the parameters of the anode sheath [37].

Although I_d is a natural boundary condition of a 1S electron model, the control of the discharge voltage V_d is more common in practice. When the external circuit fixes V_d instead of I_d, an iteration on I_d must be carried out so that $V_d(I_d)$ converges to the desired value. In certain cases, when this convergence has been elusive or fragile because of numerical instabilities, strategies based on fixing the discharge power, $P_d(I_d) = I_d V_d$, have been successful [49]. Additional convergence issues can arise in 2S thrusters, depending on the constraints imposed by the external circuit on the intermediate electrode.

The electron formulation presented here allows the implementation of other cathode models and plume boundary conditions. The *wall cathode model* formulated in [37, Sec. III] is one of them. It consists of taking $I_P = 0$ in (42) and placing an emissive annular cathode at a wall location of the near plume. Electrons injected at this cathode spread quickly along the *neutralization band* formed by the stream surfaces intersecting the cathode. Thus, the discharge can be considered 2S with a "main (inner) stage" between the anode and the cathode and an "outer stage" extending beyond the cathode location.

The wall cathode model tries to approach the actual physics of the cathode/plasma interaction and facilitates the simulation of the plume region beyond the cathode, where the magnetic field vanishes; there lies generally the upstream boundary of simulation codes of the external plume. However, the convergence of the wall cathode model is sometimes difficult to achieve, because of the high sensitivity of the sheath solution to variations in the parameters. A practical alternative to the wall cathode model, which avoids largely its numerical instabilities, is the *volumetric cathode model* presented in [49, Sec. III]. In this model, extra source terms are added to the electron fluid equations in order to model directly the neutralization band. This model behaves much better numerically and yields a plasma response that is very similar to the wall cathode model.

B. Numerical Method

The energy equation (32) is first transformed in a nonconservative equation for the temperature advection. This one is discretized spatially with first-order finite differences, whereas an explicit Euler scheme is used for the temporal discretization [i.e., forward in time and centered in space (FTCS)]. In order to preserve the order of the numerical error on λ of the FTCS scheme, a second-order accurate Adams–Bashforth method is used for the discretization of the ordinary differential equations governing the electron current and the thermalized potential [(14) and (22)]. This method must take into account that the λ-intervals are not uniform. An additional spatial discretization is used along the streamlines in order to compute the χ-integral coefficients present in the formulation. Fig. 1(c) shows a typical mesh on λ and χ.

Since the FTCS method is conditionally stable for diffusion-dominated problems, the electron time step δt is constrained to values on the order of $5 \cdot 10^{-10}$ s so that numerical stability is preserved. This value is more than two orders of magnitude lower than the time step Δt used by the PIC subcode. However, it prevents any numerical instability even in those regions where the advection term dominates over the heat diffusion term. Hence, around 200 temporal advances are carried out in each execution of the electron subcode. This is a disadvantage of this numerical method that causes an increase in the time required to carry out the simulations. In any case, the overall time spent by the simulation in the PIC and electron subcodes is comparable.

The proposed differential formulation allows the implementation of more accurate and faster numerical methods in a relatively simple way. In particular, an implicit unconditionally stable scheme, as the one proposed by Hagelaar *et al.* [31], would permit the use of the same time step in the electron and PIC subcodes. Another possible improvement would be the use of a finite-volume approach since it is more suited for conservation laws like (32). However, current results are rather acceptable in terms of overall energy conservation, as shown in Section V.

C. Comparison With Other Models

The proposed electron model improves the previous ones by Fife [10] and Parra *et al.* [12] in several ways. First, the conservation equations admit exchanges of electric current through the lateral walls, making the resulting code applicable to multistage and TAL-type Hall thrusters. Second, a sheath model for active electrodes has been added. Third, the formulation of the energy equation as a standard parabolic equation facilitates the interpretation and evaluation of the different physical phenomena involved in it. It also eases the implementation of more accurate and stable integration schemes, such as the implicit method of Hagelaar *et al.* [31]. Fourth, the formulation is more accurate since no approximation has been made in the derivation of the energy conservation equation on λ, where the work of the electric field is computed exactly. Fifth, the 2-D character of the model (for regular magnetic topologies) has been fully developed with the determination of the whole electron current density vector $\boldsymbol{j}_e$. Finally, the comparison of this differential formulation with r-averaged axial models [14], [17] is simpler. In particular, the present model recovers the 2S 1-D fluid model of Ahedo and Parra [1] in the steady-state case except for the work of the parallel electric field.

Our model keeps the restriction of dealing with regular magnetic topologies (although singular topologies could be handled by matching different regular subdomains). This restriction is removed by Pérez-Luna *et al.* [2], who solve (10)–(12), and (30) directly in the cylindrical frame. For regular magnetic topologies, where the two models are comparable, there are two main differences. First, the use of (9) lowers significantly, in our case, the computational cost by separating the computation of T_e and ϕ from that of $\boldsymbol{j}_e$, which is then reduced to simple quadratures along the streamlines. Second, Pérez-Luna *et al.* do not couple the quasi-neutral electron model to a sheath model.

Instead of our term $\sum(h_{en})$ in (32), they have a volumetric term $\langle n_e \rangle W(T_e)$ with

$$W(T_e, T_0) = \nu_W T_e \exp(-T_0/T_e) \tag{43}$$

where ν_W and T_0 are adjustable parameters. This function does not agree with the scaling law (38) for a dielectric wall, and is certainly less suitable for the energy fluxes at the sheath edge of an active electrode, where (40) applies. Finally, $\sum(h_{en})$ adds contributions from the inner and outer walls, which can be quite different when the walls are, for instance, an active electrode and a dielectric material.

VI. Results and Discussion

Results for both 1S and 2S configurations are presented here in order to illustrate the new features of the electron formulation, the importance of the sheath models, and the sensitivity of the thruster performances to changes in the lateral walls. However, neither a deep comparison with experimental results nor a parametric study of different operation parameters is carried out.

Simulations are performed for the SPT-100 thruster of Fig. 1(a). Nominal operation conditions are $V_d = 300$ V, $\dot{m}_A \approx 4.85$ mg/s of xenon, and the magnetic topology of Fig. 1(d). The PIC subcode mesh is shown in Fig. 1(a), whereas the magnetic grid used by the electron subcode is shown in Fig. 1(c). The cathode electrons are injected in the plume boundary at $T_{eP} = 5.5$ eV, i.e., neither the volumetric cathode nor the wall cathode models are used. Ceramic walls and total electron thermalization are assumed as well. Ceramics walls are characterized by $E_1 = 47.7$ eV, with E_1 being the energy of a monoenergetic beam yielding 100% of SEE, which corresponds to a crossover temperature $T_1 \simeq 32$ eV. Regarding the mass and heat transport of electrons, $\alpha_{\rm turb} \approx 0.01$ and $\alpha_q = 1$ are kept constant in all simulations.

Most of the results shown hereafter are time averages. These results are obtained by averaging 0.5 ms of simulation after a transitory period of 0.2 ms. Previous experiences have shown this methodology to yield results less than 1% different with respect to simulations that are five times longer.

In the 2S configurations, the intermediate electrode exchanges a current I_{d1} with the surrounding plasma, and the electrode-to-anode potential is V_{d1}. If I_{d2} is the current exchanged by the external cathode, the discharge current at the anode is $I_d = I_{d1} + I_{d2}$, and the discharge power is

$$P_d = I_{d2}V_d + I_{d1}V_{d1} \equiv I_d V_d - I_{d1}(V_d - V_{d1}). \tag{44}$$

In all cases, the discharge voltage V_d is used as fixed operation parameter. The cathode current I_{d2}, being the natural boundary condition, must be iterated until the desired value of V_d is achieved. Simulations with an active electrode are run at fixed current I_{d1} instead of at fixed voltage V_{d1}. The reason is the large slope in the current–voltage characteristic of an active electrode, with $\partial \ln j_{nQ}/\partial \ln \phi_{WQ} \gg 1$ (Fig. 2). This is the same argument one has for simulating the anode-to-cathode circuit with fixed V_d instead of a fixed I_{d2}. Thus, V_{d1} is an output of the simulation, which is obtained from the solution for $\phi(z, r)$ and the electrode sheath model presented earlier. Propellant, current, voltage, plume, and thruster efficiencies are defined, respectively, as

$$\begin{aligned} \eta_u &= m_i I_{iP}/e\dot{m}_A \\ \eta_c &= I_{iP}V_d/P_d \\ \eta_v &= P_{iP}/I_{iP}V_d \\ \eta_p &= F_i^2/2\dot{m}_{iP}P_d \\ \eta &= F^2/2\dot{m}_A P_d \end{aligned} \tag{45}$$

with $\dot{m}_{iP}$, I_{iP}, and P_{iP} being the ion mass flow, beam current, and kinetic power, respectively, at the plume boundary; F being the overall thrust accounting for particle momentum and electron pressure; F_i being the thrust due to the ion beam; and the rest of the symbols as usual.

A. One-Stage Thruster

The results for the 1S thruster are presented here to discuss the relevance of the proposed formulation. These results are also used as a reference for the 2S simulations.

The performances of 1S operation shown in Table I are worse than in practice. This is mainly due to the excessive energy losses at the lateral walls inherent to the total thermalization model. The partial thermalization model under development is aimed to solve this discrepancy with experiments [49]. Nevertheless, the model can be used to analyze the influence of various operation parameters and to compare different thruster configurations, in particular, 1S with respect to 2S operation.

Table II shows the contributions of the different terms to the time-averaged energy balance and the corresponding error, when the electron energy equation (31) is expressed as

$$P_{{\rm elec},e} + P_{\rm cathode} = P_{\rm ioniz} + P_{{\rm lateral},e} + P_{{\rm anode},e}. \tag{46}$$

Here, $P_{{\rm elec},e}$ is the work of the electric field, $P_{\rm cathode}$ is the amount of energy introduced with the electron current at the plume boundary, $P_{\rm ioniz}$ represents losses due to ionization and radiation, and $P_{{\rm lateral},e}$ and $P_{{\rm anode},e}$ represent energy losses into the lateral and anode sheaths, respectively. This time-averaged balance is excellent, with an error smaller than 1% of the discharge power, which is partly due to a nonzero average of the temporal derivative. Furthermore, the corresponding estimated error is less than 0.5 W in each iteration if the temporal term is accounted for properly.

Table II also shows the time-averaged perpendicular and parallel contributions to the electric work ($P_{{\rm elec},e\perp}$ and $P_{{\rm elec},e\parallel}$, respectively). These values prove that the parallel contribution cannot be neglected in the computations. The corresponding time-averaged spatial distribution is shown in Fig. 3(a) where significant differences between the overall electric work and the perpendicular contribution are observed.

Another illustration of the influence of the parallel electric work is shown in Fig. 3(b). This figure shows the ratio between the average perpendicular thermal diffusivity and the equivalent

TABLE I
PARAMETERS OF OPERATION AND PERFORMANCES OBTAINED IN THE 1S CONFIGURATION AND SEVERAL 2S CONFIGURATIONS WITH THE ELECTRODE EXCHANGING AN ELECTRIC CURRENT I_{d1} WITH THE PLASMA. OTHER OPERATION PARAMETERS ARE $V_d = 300$ V, $\dot{m}_A \approx 4.85$ mg/s, AND $B_{r,\max} \approx 230$ G. I_{iW} IS THE ION CURRENT RECOMBINED AT THE LATERAL WALLS. [1] INDICATES THAT THE MAGNETIC FIELD STRENGTH HAS BEEN INCREASED UNTIL THE DISCHARGE POWER EQUALS THAT OF THE 2S FLOATING ELECTRODE CASE. [2] CORRESPONDS TO A SIMULATION WITH A 2-mm-THICK ELECTRODE CENTERED AT 16 mm FROM THE ANODE

$I_{d1}(A)$	$I_{d2}(A)$	$P_d(W)$	$V_{d1}(V)$	$I_{iW}(A)$	$I_{iP}(A)$	η	η_c	η_u	η_v	η_p
-	4.17	1250	-	1.67	3.16	0.391	0.76	0.85	0.83	0.69
0.0	4.05	1214	65.4	0.82	3.30	0.481	0.82	0.90	0.84	0.76
0.51	4.07	1255	66.7	0.91	3.33	0.490	0.80	0.91	0.86	0.77
1.02	4.07	1290	67.6	1.03	3.34	0.498	0.78	0.91	0.88	0.78
1.54	4.05	1324	70.8	1.17	3.33	0.497	0.75	0.91	0.89	0.78
2.05	4.01	1354	73.7	1.35	3.32	0.493	0.73	0.91	0.90	0.79
[1]1.02	3.77	1214	81.4	0.89	3.33	0.543	0.82	0.91	0.88	0.80
-0.51	4.00	1170	58.8	0.79	3.26	0.451	0.84	0.88	0.80	0.74
[2]1.12	4.15	1329	75.0	1.24	3.36	0.496	0.76	0.91	0.90	0.78

TABLE II
TIME-AVERAGED VALUES OF THE CONTRIBUTIONS TO THE ELECTRON ENERGY BALANCE FOR THE 1S CASE

$P_{elec,e}$	$P_{elec,e\perp}$	$P_{elec,e\parallel}$	$P_{cathode}$	P_{ioniz}	$P_{lateral,e}$	$P_{anode,e}$	Error
557.3 W	806.7	-249.4	8.0 W	152.1 W	348.0 W	73.4 W	1.8 W

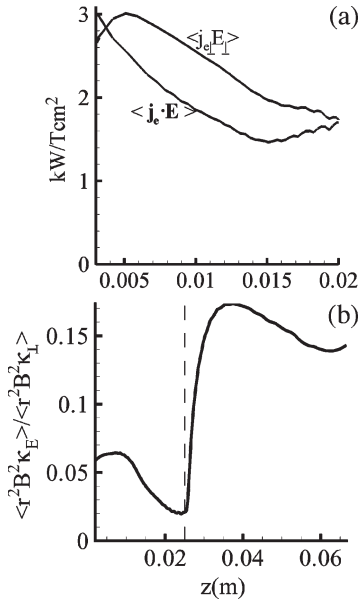

Fig. 3. (a) Overall and perpendicular electric work. (b) Ratio between the average perpendicular thermal diffusivity $\kappa_\perp$ and the equivalent thermal diffusivity due to the parallel electric work κ_E along the channel median. Note that the z-scales are different in these figures, and the units in (a) are associated to the magnetic integral operator. The dashed line in (b) represents the thruster chamber exit plane. Results correspond to the 1S configuration.

thermal diffusivity due to $\langle j_{e\parallel} E_\parallel \rangle$. This ratio is greater than 15% in the near plume where 2-D effects are quite significant due to the important variation of the plasma density along the streamlines. Inside the thruster chamber, this ratio is smaller, although it can be up to 6% near the anode. Notice that the influence of κ_E would be larger if thermal diffusivity were partially inhibited with respect to mass diffusivity, i.e., if α_q in (24) were less than one.

B. Two-Stage Thruster

A 2S configuration built with a 5-mm-thick annular electrode placed on the outer wall and centered at 15 mm from the anode [Fig. 1(a)] is analyzed here. Its location follows the common 2S design, where the electrode is placed between the ionization and acceleration regions. The magnetic field topology is unchanged with respect to the 1S simulations.

The 1-D fully fluid model of Ahedo and Parra [1] for 2S discharges showed that an ideal electron-emitting electrode can enhance significantly the efficiency of the plasma discharge if the electrode is located and biased conveniently, and the magnetic field is adjusted too. In their simulations, the optimal electrode-to-anode distance was around 15 mm for a SPT-100 thruster under the operation conditions considered here. Based on this work, the same location has been used in this paper, and the strength of the magnetic field is modified in order to optimize the thruster performances in 2S operation. Table I and Figs. 4–7 show results of the simulations carried out for the 1S configuration of reference and several 2S cases with varying electrode current.

For $I_{d1} = 0$, the electrode is at floating potential. Observe in Table I the differences in performance between this case and the 1S case: The ion current lost into the lateral walls (I_{iW}) has been reduced to about one-half, and the thrust efficiency has been increased significantly. This illustrates the large sensitivity of the plasma discharge to the interaction with the walls. In this case, a 5-mm segment of the ceramic wall, with a moderate SEE ($\sim$73%), is substituted by a high-emission electrode, which has a stronger contact with the plasma: The sheath potential fall satisfies $e\phi_{WQ}/T_e \approx 4.32$ for the 5-mm segment of ceramic wall and $e\phi_{WQ}/T_e \approx 1.13$ for the floating active electrode (Fig. 5). Since energy losses of primary electrons are proportional to $n_{eQ}\sqrt{T_e}\exp(-e\phi_{WQ}/T_e)$, the lower sheath fall for the emissive electrode implies (for the same thermal flux) a much larger energy loss. From Figs. 5 and 7, it seems that the plasma tries to reduce the impact of the low sheath fall by reducing the plasma density there. This adjustment modifies ultimately a large part of the density and temperature profiles (Figs. 5 and 7). As a result, the energy losses to the inner wall are much lower for the floating 2S configurations than for the 1S one (Fig. 5). Curiously, the different trends of n_e

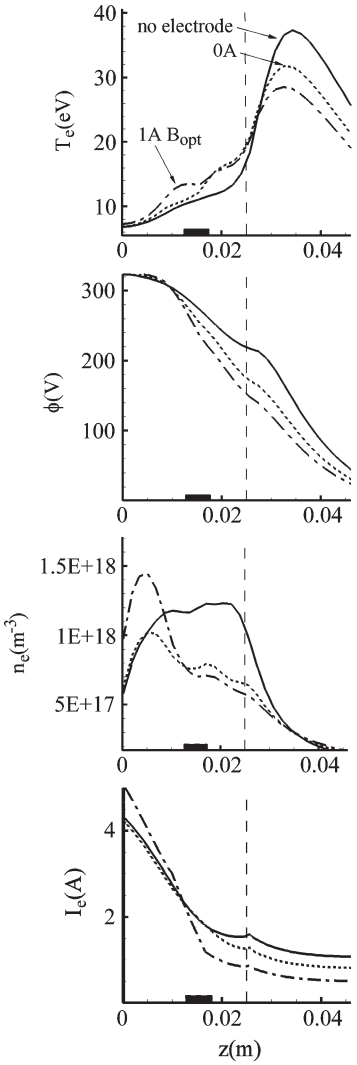

Fig. 4. One-dimensional (time-averaged) plasma profiles at the channel median for the 1S thruster and a 2S thruster with the intermediate electrode placed at $z = 15$ mm and emitting different electric currents I_{d1}'s.

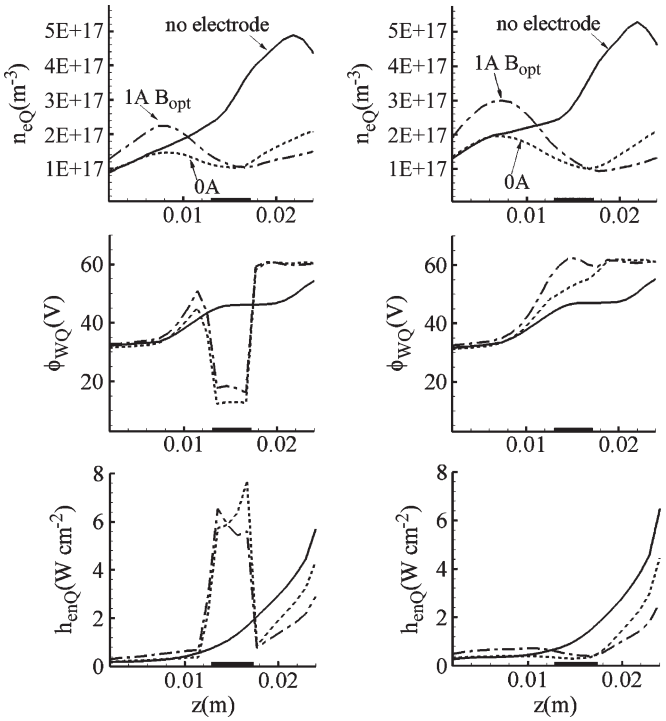

Fig. 5. One-dimensional plasma profiles at the (left plots) outer and (right plots) inner sheath and wall for the same cases than Fig. 4.

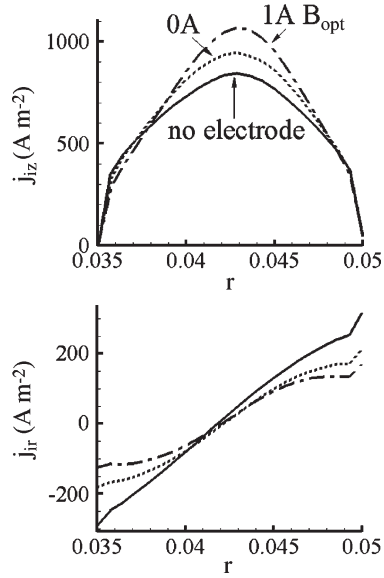

Fig. 6. Axial and radial ion current densities at the chamber exit section for the same configurations than Fig. 4.

and T_e result in similar profiles for the ionization source $\dot{n}_i$. A consequence of keeping almost the same $\dot{n}_i$ and the reduction of the ion current to the wall is a larger axial ion current density in the plume and a smaller radial current (Fig. 6), which would result in a lower plume divergence. This is consistent with the increased plume efficiency reported in Table I.

In order to assess the influence of the electrode current, a parametric variation has been carried out on I_{d1}, ranging from 0 to 2 A. Results in Table I indicate a small improvement in the overall efficiency for the $I_{d1} = 1$ A case with respect to the floating electrode configuration due to an enhanced acceleration process (η_v) compensated by the decrease of the current efficiency (η_c). This suggests that the magnetic field should be optimized for this 2S case. Then, as the electrode current continues to increase, efficiency drops slowly, possibly because the main ionization takes place too upstream and the increase of losses to the walls.

The optimization of the magnetic strength is carried out on the $I_{d1} = 1$ A case since its performance is the best among the previous 2S simulations at constant magnetic field. In order to compare properly thruster performances, the magnetic field strength is increased until the discharge power P_d [(44)] equals the floating electrode case. An increase of 25% suffices to achieve this goal. Performance results shown in Table I indicate that a relevant efficiency improvement is achieved for the same P_d and $\dot{m}_A$ as in the 2S floating electrode case. This improved performance comes from the enhanced current utilization, which does not affect negatively the ionization and acceleration processes. Similar conclusions were obtained by Ahedo and Parra [1] with their 1-D fluid model.

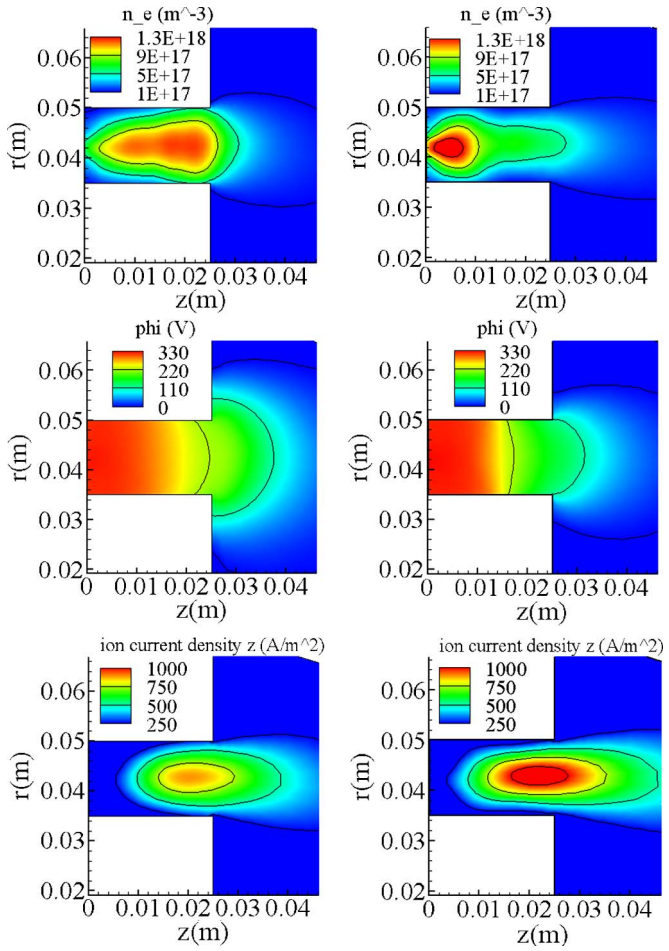

Fig. 7. Two-dimensional plasma maps of n_e, ϕ, and j_{iz} for (left plots) the 1S configuration and (right plots) the 1A-$B_{\rm opt}$ 2S configuration of Figs. 4 and 5, respectively.

Ahedo and Parra [1] find that the electron-collecting mode leads always to efficiency deterioration. A 2S simulation of the electron-collecting mode, $I_{d1} = -0.5$ A, is reported in Table I and confirms the quick decrease of efficiency in this mode. This is explained by the fact that part of the electron current emitted by the cathode is heated up in the acceleration region but is collected by the electrode before ionizing the gas. Pérez-Luna *et al.* [2] have also simulated 2S configurations in the electron-collecting mode. In their study, a doubly peaked magnetic field is used, and the electrode control parameter is the anode-to-electrode potential, with the electrode current being an output of the simulation. However, they do not use a sheath model for the active electrode, and thus, the potential that they are actually fixing *is not* the electrode potential, $\phi_W = V_d - V_{d1}$, but the sheath edge potential, $\phi_Q = V_d - V_{d1} + \phi_{WQ}$, which, in practice, is self-adjusted by the plasma. Curiously, they find that the electrode cannot operate in the electron-emitting mode within a reasonable range of physical parameters. One possible explanation is that they place the electrode between the two magnetic peaks, where the magnetic streamlines are near-parallel to the electrode instead of near-perpendicular. This would force the electrode to act as an extra anode rather than as an intermediate cathode.

A characteristic of the intermediate electrode which is found to be more relevant than expected from the Ahedo–Parra model is its surface A_{ae}. For a fixed electrode current I_{d1}, the injected electric current density is inversely proportional to that surface ($j_{nQ} = I_{d1}/A_{ae}$). Then, for fixed plasma conditions, one has $j_{nQ}/j_{inQ} \propto A_{ae}^{-1}$, and (40) states that the smaller the electrode surface is, the deeper the electrode operates in the emission mode and the more favorable the energy exchange at the sheath edge is. For instance, in the simulation for $I_{d1} = 1.5$ A with the 5-mm electrode placed at the outer wall, we have $j_{nQ}/j_{inQ} \sim 22$, and $T_e \sim 14$ eV, which means that $\int_{A_{ae}} h_{enQ} dA \sim 100$ W. For the same plasma conditions and the 1-mm-thick electrode, it would be $j_{nQ}/j_{inQ} \sim 110$ and $\int_{A_{ae}} h_{enQ} dA \sim -140$ W, i.e., the electrode delivers energy into the bulk of the plasma. As an example, performances corresponding to a simulation with a 2-mm electrode in the outer wall centered at 16 mm from the anode are shown in Table I.

Ahedo and Parra consider the active electrode to be infinitely thin. Then, no electrode sheath needs to be considered, with the energy exchange with the sheath being included as a source term in the 1-D equations (proportional to $-I_{d1}$), and since the model is 1-D, the electrode potential V_{d1} is approximated by the radially averaged plasma potential (quite similarly to the way Pérez-Luna *et al.* treat the electrode in their otherwise 2-D quasi-neutral model). Therefore, an infinitely thin electrode operates only on the "high" emission and collection modes. Furthermore, the floating mode coincides exactly with the 1S configuration since $\int_{A_{ae}} h_{enQ} dA = 0$.

VII. Conclusion

The 2-D electron model presented here features relevant improvements over the previous version implemented in a hybrid code for Hall thrusters, which have been summarized already in Section V-C. The main one is the admission of exchange of electric current through lateral walls and segmented electrodes, which augments significantly the range of application of the resulting hybrid code. In order to illustrate the code's new capabilities, 2S configurations with an intermediate active electrode have been simulated and analyzed. The electrode can operate in (negative)-current-emission and collection modes, as well as in the floating mode. In the high-emission and collecting modes, results coincide practically with those of Ahedo and Parra with a 1-D fully fluid model and an infinitely thin electrode. Thus, 2-D simulations confirm that efficiency increases promisingly in the emission mode if the magnetic field strength is optimized; efficiency decreases in the collection mode, since the intermediate electrode acts as a first anode which collects electrons before they reach the ionization region. Nonetheless, two-dimensionality and electrode finite-size bring up features not unveiled by the Ahedo–Parra model. The most illustrative example is the large differences between the 1S and the floating-mode 2S responses. The stronger plasma–electrode contact of a thick active electrode in the floating mode modifies globally the temperature and density profiles, resulting in lower energy loss and plume divergence, and a larger efficiency.

To conclude, the simulations here illustrate on the potential benefits of segmented electrodes in order to shape the plasma response and enhance thruster performances. At the same time, they show plasma behaviors which are not evident from our

understanding of 1S discharges. For us, this is another proof of the strong nonlocal coupling among the various physical phenomena competing in a Hall thruster plasma and one of the reasons to explain the difficulties on succeeding with 2S prototypes. In order to assess correctly the plasma response in multistage discharges, a more profound and systematic investigation needs to be carried out, including a wider group of electrodes. This will also allow one to contrast this 2S model with the large set of experiments carried out by Raitses *et al.* [5]–[7] with different segmented electrodes in different configurations, where many aspects are needed of interpretation yet. For the moment, the model and experiments are not at odds at least in the following two aspects: the possibility of plume divergence reduction with segmented electrodes and the large sensitivity of the plasma to wall and electrode conditions.

ACKNOWLEDGMENT

The authors would like to thank F. Parra for the insightful discussions.

REFERENCES

[1] E. Ahedo and F. I. Parra, "A model of the two-stage Hall thruster discharge," *J. Appl. Phys.*, vol. 98, no. 2, pp. 023 303-1–023 303-11, Jul. 2005.

[2] J. Pérez-Luna, G. J. M. Hagelaar, L. Garrigues, and J. P. Boeuf, "Model analysis of a double-stage Hall effect thruster with double-peaked magnetic field and intermediate electrode," *Phys. Plasmas*, vol. 14, no. 11, pp. 113 502-1–113 502-10, Nov. 2007.

[3] H. R. Kaufman, "Technology of closed-drift thrusters," *AIAA J.*, vol. 23, no. 1, pp. 78–87, Jan. 1985.

[4] R. R. Hofer, P. Y. Peterson, A. D. Gallimore, and R. S. Jankovsky, "A high specific impulse two-stage Hall thruster with plasma lens focusing," presented at the 7th Int. Electric Propulsion Conf., Pasadena, CA, 2001, IEPC-01-036.

[5] Y. Raitses, L. A. Dorf, A. A. Litvak, and N. J. Fisch, "Plume reduction in segmented electrode Hall thruster," *J. Appl. Phys.*, vol. 88, no. 3, pp. 1263–1270, Aug. 2000.

[6] N. J. Fisch, Y. Raitses, L. A. Dorf, and A. A. Litvak, "Variable operation of Hall thruster with multiple segmented electrodes," *J. Appl. Phys.*, vol. 89, no. 4, pp. 2040–2046, Feb. 2001.

[7] Y. Raitses, D. Staack, and N. J. Fisch, "Plasma characterization of Hall thruster with active and passive segmented electrodes," presented at the 38th Joint Propulsion Conf., Indianapolis, IN, 2002, AIAA-2002-3954.

[8] Y. Yamagiwa and K. Kuriki, "Performance of double-stage-discharge Hall ion thruster," *J. Propuls. Power*, vol. 7, no. 1, pp. 65–70, Jan./Feb. 1991.

[9] B. Pote and R. Tedrake, "Performance of a high specific impulse Hall thruster," presented at the 27th Int. Electric Propulsion Conf., Pasadena, CA, 2001, IEPC-01-035.

[10] J. M. Fife, "Hybrid-PIC modeling and electrostatic probe survey of Hall thrusters," Ph.D. dissertation, MIT, Cambridge, MA, 1998.

[11] J. C. Adam, A. Herón, and G. Laval, "Study of stationary plasma thrusters using two-dimensional fully kinetic simulations," *Phys. Plasmas*, vol. 11, no. 1, pp. 295–305, Jan. 2004.

[12] F. I. Parra, E. Ahedo, J. M. Fife, and M. Martínez-Sánchez, "A two-dimensional hybrid model of the Hall thruster discharge," *J. Appl. Phys.*, vol. 100, no. 2, pp. 023 304-1–023 304-11, Jul. 2006.

[13] E. Ahedo, "Presheath/sheath model with secondary electron emission from two parallel walls," *Phys. Plasmas*, vol. 9, no. 10, pp. 4340–4347, Oct. 2002.

[14] E. Ahedo, J. M. Gallardo, and M. Martínez-Sánchez, "Effects of the radial plasma–wall interaction on the Hall thruster discharge," *Phys. Plasmas*, vol. 10, no. 8, pp. 3397–3409, Aug. 2003.

[15] F. I. Parra and E. Ahedo, "Fulfillment of the Bohm condition on the HPHall fluid-PIC code," presented at the 40th Joint Propulsion Conf., Fort Lauderdale, FL, 2004, AIAA 2004-3955.

[16] N. B. Meezan and M. A. Capelli, "Kinetic study of wall collisions in a coaxial Hall discharge," *Phys. Rev. E, Stat. Phys. Plasmas Fluids Relat. Interdiscip. Top.*, vol. 66, no. 3, p. 036 401, Sep. 2002.

[17] S. Barral, K. Makowski, Z. Peradzynski, N. Gascon, and M. Dudeck, "Wall material effects in stationary plasma thrusters. II. Near-wall and in-wall conductivity," *Phys. Plasmas*, vol. 10, no. 10, pp. 4137–4152, Oct. 2003.

[18] E. Ahedo and F. I. Parra, "Partial trapping of secondary-electron emission in a Hall thruster plasma," *Phys. Plasmas*, vol. 12, no. 7, p. 073 503, Jun. 2005.

[19] I. D. Kaganovich, Y. Raitses, D. Sydorenko, and A. Smolyakov, "Kinetic effects in a Hall thruster discharge," *Phys. Plasmas*, vol. 14, no. 5, pp. 057 104-1–057 104-11, May 2007.

[20] F. Taccogna, S. Longo, and M. Capitelli, "Plasma sheaths in Hall discharge," *Phys. Plasmas*, vol. 12, no. 9, pp. 093 506-1–093 506-14, Sep. 2005.

[21] D. Sydorenko, A. Smolyakov, I. Kaganovich, and Y. Raitses, "Kinetic simulation of secondary electron emission effects in Hall thrusters," *Phys. Plasmas*, vol. 13, no. 1, pp. 014 501-1–014 501-4, Jan. 2006.

[22] E. Ahedo and V. de Pablo, "Combined effects of electron partial thermalization and secondary emission in Hall thruster discharges," *Phys. Plasmas*, vol. 14, no. 8, p. 083 501, Aug. 2007.

[23] J. M. Fife and M. Martínez-Sánchez, "Comparison of results from a two-dimensional numerical SPT model with experiment," presented at the 32nd Joint Propulsion Conf., Lake Buena Vista, FL, 1996, AIAA-1996-3197.

[24] J. J. Szabo, M. Martínez-Sánchez, and J. Monheiser, "Application of 2-D hybrid PIC code to alternative Hall thruster geometries," presented at the 34th Joint Propulsion Conf., Cleveland, OH, 1998, AIAA-1998-3795.

[25] E. Ahedo, I. Maqueda, A. Antón, Y. Raitses, and N. Fisch, "Numerical simulations of a 2kW Hall thruster," presented at the 42th Joint Propulsion Conf., Sacramento, CA, 2006, AIAA-2006-4655.

[26] D. Escobar, A. Antón, and E. Ahedo, "Simulation of high-specific-impulse and double-stage Hall thrusters," presented at the 29th Int. Electric Propulsion Conf., Princeton, NJ, 2005, IEPC-2005-040.

[27] M. Gamero-Castaño and I. Katz, "Estimation of Hall thruster erosion Using HPHall," presented at the 29th Int. Electric Propulsion Conf., Princeton, NJ, 2005, IEPC-2005-303.

[28] E. Ahedo, A. Antón, I. Garmendia, I. Caro, and J. González del Amo, "Simulation of wall erosion in Hall thrusters," presented at the 30th Int. Electric Propulsion Conf., Florence, Italy, 2007, IEPC 2007-067.

[29] R. Hofer, I. Mikellides, and I. Katz, "BPT-4000 hall thruster discharge chamber erosion model comparison with qualification life test data," presented at the 30th Int. Electric Propulsion Conf., Florence, Italy, 2007, IEPC-2007-267.

[30] S. Cheng and M. Martinez-Sanchez, "Modeling of Hall thruster lifetime and erosion mechanisms," presented at the 30th Int. Electric Propulsion Conf., Florence, Italy, 2007, IEPC-2007-250.

[31] G. J. M. Hagelaar, J. Bareilles, L. Garrigues, and J. P. Boeuf, "Two-dimensional model of a stationary plasma thruster," *J. Appl. Phys.*, vol. 91, no. 9, pp. 5592–5598, May 2002.

[32] J. P. Boeuf and L. Garrigues, "Low frequency oscillations in a stationary plasma thruster," *J. Appl. Phys.*, vol. 84, no. 7, pp. 3541–3554, Oct. 1998.

[33] M. K. Scharfe, N. Gascon, M. A. Cappelli, and E. Fernandez, "Comparison of hybrid Hall thruster model to experimental measurements," *Phys. Plasmas*, vol. 13, no. 8, pp. 083 505-1–083 505-12, Aug. 2006.

[34] G. J. Hagelaar, "Modelling electron transport in magnetized low-temperature discharge plasmas," *Plasma Sources Sci. Technol.*, vol. 16, no. 1, pp. 57–66, Jan. 2007.

[35] D. Escobar and E. Ahedo, "Improved electron formulation for a Hall thruster hybrid model," presented at the 42th Joint Propulsion Conf., Sacramento, CA, 2006, AIAA-2006-4326.

[36] F. Parra, D. Escobar, and E. Ahedo, "Improvements on particle accuracy in a Hall thruster hybrid code," presented at the 42th Joint Propulsion Conf., Sacramento, CA, 2006, AIAA-2006-4830.

[37] A. Antón, D. Escobar, and E. Ahedo, "Contour algorithms for a Hall thruster hybrid code," presented at the 42th Joint Propulsion Conf., Sacramento, CA, 2006, AIAA-2006-4834.

[38] R. D. Hazeltine and J. D. Meiss, *Plasma Confinement*. Redwood City, CA: Addison-Wesley, 1992.

[39] J. M. Haas and A. D. Gallimore, "An investigation of internal ion number density and electron temperature profiles in a laboratory-model hall thruster," presented at the 36th Joint Propulsion Conf., Huntsville, AL, 2000, AIAA 2000-3422.

[40] E. Ahedo and D. Escobar, "Two-region model for positive and negative plasma sheaths and its application to Hall thruster metallic anodes," *Phys. Plasmas*, vol. 15, no. 3, p. 033 504, Mar. 2008.

[41] G. F. Chew, M. L. Goldberger, and F. E. Low, "The Boltzmann equation and the one-fluid hydromagnetic equations in the absence of particle collisions," *Proc. R. Soc. Lond. A, Math. Phys. Sci.*, vol. 236, no. 1204, pp. 112–118, Jul. 1956.

[42] J. J. Ramos, "Fluid formalism for collisionless magnetized plasmas," *Phys. Plasmas*, vol. 12, no. 5, pp. 052 102-1–052 102-14, May 2005.
[43] G. S. Janes and R. S. Lowder, "Anomalous electron diffusion and ion acceleration in a low-density plasma," *Phys. Fluids*, vol. 9, no. 6, pp. 1115–1123, Jun. 1966.
[44] A. I. Morozov, Y. V. Esipchuk, G. N. Tilinin, A. V. Trofimov, Y. A. Sharov, and G. Y. Shchepkin, "Plasma accelerator with closed electron drift and extended acceleration zone," *Sov. Phys.—Tech. Phys.*, vol. 17, no. 1, pp. 38–45, Jul. 1972.
[45] E. Ahedo, V. de Pablo, and M. Martínez-Sánchez, "Effects of partial thermalization and secondary emission on the electron distribution function of Hall thrusters," presented at the 29th Int. Electric Propulsion Conf., Princeton, NJ, 2005, IEPC-2005-118.
[46] G. J. M. Hagelaar, J. Bareilles, L. Garrigues, and J. P. Boeuf, "Role of anomalous electron transport in a stationary plasma thruster simulation," *J. Appl. Phys.*, vol. 93, no. 1, pp. 67–75, Jan. 2003.
[47] J. W. Koo and I. D. Boyd, "Modeling of anomalous electron mobility in Hall thrusters," *Phys. Plasmas*, vol. 13, no. 3, pp. 033 501-1–033 501-7, May 2006.
[48] J. Fox, A. A. Batishcheva, O. V. Batishchev, and M. Martinez-Sanchez, "Adaptively meshed fully-kinetic PIC–Vlasov model for near vacuum hall thrusters," presented at the 42th Joint Propulsion Conf., Sacramento, CA, 2006, AIAA 2006-4324.
[49] I. Maqueda, D. Escobar, and E. Ahedo, "Advances on a Hall thruster hybrid code," presented at the 30th Int. Electric Propulsion Conf., Florence, Italy, 2007, IEPC 2007-066.
[50] D. Escobar, E. Ahedo, and F. I. Parra, "On conditions at the sheath boundaries of a quasineutral code for Hall thrusters," presented at the 29th Int. Electric Propulsion Conf., Princeton, NJ, 2005, IEPC-2005-041.
[51] M. A. Raadu, "The physics of double layers and their role in astrophysics," *Phys. Rep.*, vol. 178, no. 2, pp. 26–97, Apr. 1989.

Diego Escobar received the Diploma and Advanced Studies degrees in aeronautical engineering from the Universidad Politécnica de Madrid, Madrid, Spain, in 2005 and 2007, respectively.

From 2005 to 2007, he was a Part-Time Student combining his studies with a professional experience at GMV S.A. He is currently a Contractor Staff with the European Space Operations Center, European Space Agency, Darmstadt, Germany. His research background includes modeling and simulation in Hall thrusters and satellite orbit dynamics and navigation in the professional field.

Eduardo Ahedo received the Diploma and Doctorate degrees in aeronautical engineering from the Universidad Politécnica de Madrid (UPM), Madrid, Spain, in 1982 and 1988, respectively. From 1989 to 1990, he was a Postdoctoral Scholar with the Massachusetts Institute of Technology, Cambridge, MA.

He is currently a Professor of aerospace engineering with the Escuela Técnica Superior de Ingenieros Aeronáuticos, UPM. His research background includes modeling and simulation in plasma propulsion, electrodynamic tethers, plasma contactors, plasma–surface interactions, plasma instabilities, and plasma–laser interactions.